Parameterization of Snowpack Albedo Reduction by Light-Absorbing Impurities

Hoi Ga Chan
Princeton University

Paul Ginoux
NOAA/Geophysical Fluid Dynamics Laboratory

Sergey Malyshev
NOAA/Geophysical Fluid Dynamics Laboratory

Sarah Kapnick
NOAA/Geophysical Fluid Dynamics Laboratory

25 August 2022

GFDL Biogeochemistry, Atmospheric Chemistry, and Ecosystems Division
Technical Memorandum GFDL202203

Abstract

Light-absorbing impurities (LAIs) deposited on snow surfaces can accelerate melt by increasing solar radiation absorption through snow darkening and grain metamorphism. To improve the predictive capability of the global impact of LAIs on the surface energy balance, we have developed a simple snow parameterization - Snow LAI Redistribution (SLAIR) to estimate the snow albedo based on the concentration of LAIs and grain size. The parameterization can be run as a standalone model constrained by temperature, snowfall, ablation, and aerosol deposition or be implemented into large scale models. The concentration of LAIs at the snow surface depends on aerosol deposition and vertical redistribution during melt. To represent the uncertainties associated with different melting regimes, two approaches were considered, one assuming all the meltwater is contributed from the top of the snowpack ("surface melt mode") and one assuming each snow layer contributes the same fraction of the mass of the total melt ("uniform melt mode"). The parameterization is evaluated as a standalone model against publicly available data at the French Alps using observational inputs. The paramterization captured the temporal variations in grain size but not the detailed variabilities. For concentration of LAIs and visible albedo, both melting modes agree reasonably well with observations during the accumulation phase but only the surface melt model reproduced observations with good agreement. Overall, the simple snow parameterization can estimate the near-surface concentration of LAIs, grain size and visible albedo within a reasonable range. Further developments are required to minimize uncertainties, especially for relatively warm and humid regions.

Plain Language Summary

Light-absorbing impurities (LAIs) deposited on snow or ice surface can accelerate melt by increasing absorption of solar radiation directly through changing the color of snow and indirectly through altering the size and shape of the snow grains. Changes in the timing and quantity of the melt can have implications on water security and cause hazards in snow-dominated regions. However, the impacts of snow darkening by LAIs are not well described in large-scale models. Here, we present a simple snow parameterization to estimate the surface albedo based on the concentration of LAIs and snow grain size at the near-surface of the snowpack. The parameterization was evaluated against a snow-year-long field observation in Col de Porte, French Alps. It suggested the parameterization can provide a reasonable estimation of the near-surface concentration of LAIs, snow grain size, and visible albedo of surface snow.

1 Introduction

Snow cover has a strong impact on the surface energy budget and atmospheric circulation due to its high reflectivity relative to underlying surfaces and high heat-insulation property. In snow-dominated regions, snow also acts like a natural water tower, which stores winter precipitation and release it gradually in spring with rising temperature and as the primary source of freshwater (Brown et al., 2014). Changes in the timing and quantity of the melt can have implications on water and food security, local ecosystems, hydropower generation, hazards associated with landslides, and outburst floods during rapid melt events. The mass and extent of snow cover are declining globally in the last decade (Estilow et al., 2015). The decline in snow cover is mainly related to the warming climate and change of precipitation patterns (Kapnick & Delworth, 2013b) but has also been linked to snow surface darkening from light-absorbing impurities (LAIs), such as mineral dust (dust), black carbon (BC), organic carbon (OC), and microbial cells that are deposited or grow on the snow/ice surface (Skiles et al., 2018). LAIs can accelerate melt by directly increasing absorption of solar radiation (mostly in the visible band), and indirectly by modifying snow metamorphism and decreasing albedo as a result, especially in the infrared band. Understanding and modeling LAIs influence on snow albedo is critical to estimating changes and variability in snowpack.

Snow albedo depends on many factors, such as grain size and shape, impurities content, density, the effective angle of solar incidence, and the ratio of direct to diffuse radiation. The absorption of ice in the visible wavelength is very weak (Warren & Brandt, 2008) so that the visible albedo of snow can be reduced significantly by the presence of LAIs while the infrared albedo is more sensitive to the grain size. In general, clean fresh snow (i.e. snow that containing virtually no LAIs) has a high albedo in both visible and infrared as fresh snow grains tend to be small in size, dendritic, and non-spherical, allowing fresh snow to efficiently reflect and scatter light back to the atmosphere. The size, dendriticity, and shape of the snow grain evolve as they age. Grain growth often leads to a larger and rounder snow grain with smoother surfaces, which increases the absorption path length within the grain and reduces scattering, hence, reduces the albedo (Warren, 1982).

The impact of LAI on albedo mainly depends on the optical properties and the concentration of the LAIs. Common LAIs like BC and OC are formed during incomplete combustion of fossil fuels and biomass. BC has strong absorption in the visible light while OC is less absorptive and often consists of complex mixtures of organic compounds. Dust, another common LAI and most abundant aerosol by mass, is a natural aerosol lifted from dry and barren land to the atmosphere by wind. The absorption of dust is determined by its size and the metal (e.g. iron) content. The concentration of LAIs in snow depends on their mixing ratio in precipitation (wet deposition), the amount of aerosols deposited to the surface (dry deposition), biological growth in the snow, and post-deposition processes that redistribute the impurities in the snowpack, such as snow sublimation and melt (Conway et al., 1996). Sublimation at the snowpack surface leads to the loss of the snowpack mass to the atmosphere, which causes the LAIs to concentrate at the snow surface. Melt, however, enhances the concentration of LAIs as a result of large particle size and their hydrophobicity - particles cannot efficiently wash away with the meltwater (a scavenging efficiency $< 100\%$) retaining within the snowpack. The melt amplification is prominent in the top few centimeters of snowpack during ablation and can increase the concentration by a factor of $\sim$10-15 relative to fresh snow (Doherty et al., 2013). This enhancement in LAI concentration at the snow surface leads to an increase in temperature within the snowpack, and hence, accelerate grain growth and, indirectly, further decrease in snow albedo (Hadley & Kirchstetter, 2012). In addition to the optical properties and concentration of LAI, the size and shape of snow grain and the LAIs-snow mixing state (internal vs. external) can also reinforce the impact of LAIs on the snow albedo (He, Liou, et al., 2018).

Numerical models have been used to understand the radiative impact of LAIs on snow. Detailed internal-snow-process schemes models with multiple layers of fine vertical resolution, e.g. Crocus (Vionnet et al., 2012; Tuzet et al., 2017), that includes simulation of internal temperature, moisture, and solar radiation can track the evolution of grain microstructures, concentration and distribution of LAIs within the snowpack, and snow albedo. These detailed models are computationally costly and therefore they are usually used for point-scale and regional studies. Among large-scale Earth system or climate models, some implement coupled intermediate-complexity snow schemes with limited number of snow layers that accounts for vertically resolved snow thermal processes, compaction, water mass and LAIs transport, and snow radiative transfer model, to represent the radiative forcing of LAIs in snow, e.g. implementation of SNICAR (Flanner et al., 2009) in the National Center for Atmospheric Research Community Land Model (Lawrence et al., 2019). These type of models can quantify both the direct and indirect impacts of LAIs in snow through estimating the subsurface aerosol heating and snow aging within the snowpack, however, they might still be computational costly for high resolution and long-term global scale experiments. Some large-scale models have simple snow scheme to represent snow hydrology while the snow albedo is estimated independently by a simple snow parameterization, often as a function of surface temperature, e.g. the Geophysical Fluid Dynamics Laboratory (GFDL) Atmosphere-Land Model version 4 (AM4/LM4) (Zhao et al., 2018b) and European Centre for Medium-Range Weather Forecast model (Dutra et al., 2010), or as a tuning parameter for reproducing surface temperature. These simple descriptions of snow albedo neglect the radiative feedback of LAIs and cause uncertainties in the radiative forcing and hydroclimate response associated with snow darkening.

There is a need for a simple snow parameterization for large scale model that can represent the interactions between LAIs and snow but without increasing the model complexity. Here, we are introducing a new parameterization for estimating the surface snow albedo from simulated near-surface concentration of LAIs and grain size that base on snowfall, sublimation, melt, aerosols deposition flux, and temperature. The parameterization is developed with an aim of implementing it into large scale models that already have a satisfactory snow hydrology scheme in place or to run off-line as a standalone model using outputs from large scale model. Details of the new snow parameterization are presented in Sect. 2. The observational and modeling data used for evaluating the parameterization as a standalone model and sensitivity studies are described in Sect. 3. The results and discussion are shown in Sect. 4.

2 Parameterization Description

A simple 1D multilayer snow parameterization - Snow LAI Redistribution (SLAIR) is developed to estimate snow surface albedo based on the concentration of LAI, c_{LAI}, due to aerosols deposition and redistribution during melt, and the evolution of effective grain size, r, due to aging at the near-surface layer, h_{ns}, of a snowpack, which is a user define parameters. When the parameterization is run in the standalone mode, the parameterization is constrained by the surface temperature, $\mathrm{T_{surf}}$, daily flux of solid precipitation (snowfall), $\mathrm{F_{snowfall}}$, surface sublimation, $\mathrm{F_{sub}}$, total snowmelt, $\mathrm{F_{melt}}$, and the total (dry + wet) deposition flux of aerosols, $\mathrm{F_{LAI}}$. When implementing the parameterization into large scale model, that already have an adequate hydrology scheme in place, i.e. calculate the energy and mass balances of snow on the ground, an initial snow albedo would have be assigned to estimate the initial ablation.

2.1 LAIs representation in SLAIR

In order to represent the vertical distribution of LAIs, such as BC, dust and organic matter (OM), the snowpack can have up to 365 numerical snow layers that each have a minimum mass of $m_{min} = 0.75$ kgm^{-2}. As the parameterization is focusing on the snow surface properties, the most bottom layer will be “swept off” when the maximum number of layers is reached. The vertical structure and distribution of the snowpack is computed in three sub-steps in the order of snowfall, surface sublimation, and snowmelt (Fig. 1).

A new snow layer is created on the top of the snowpack when the fresh snow mass is larger than m_{min}. The concentration of LAIs of the new snow layer will solely depend on the aerosols deposition flux and snowfall, i.e. $c^{P1}_{LAI,N} = \mathrm{F_{LAI}}/\mathrm{F_{snowfall}}$, where N is the total number of snow layer with the N^{th} layer being the topmost and $c^{P1}_{LAI,N}$ is the post-snowfall concentration of LAI of the topmost layer. Note: snowfall is the first sub-step, denoted by “P1”. If there is no snowfall or if the fresh snow mass is less than m_{min} then the total number of snow layers will remain unchanged. In the latter case, the fresh snow and the freshly deposited aerosols are merged with the existing topmost layer and assumed instantaneously mixed. The post-snowfall LAI concentration of the topmost layer, $c^{P1}_{LAI,N}$, is calculated as

$$c^{P1}_{LAI,N} = \frac{F_{LAI} + c_{LAI,N}(t)m_N(t)}{F_{snowfall} + m_N(t)} \tag{1}$$

where $c_{LAI,N}(t)$ and $m_N(t)$ are the concentration of one of the species and the mass of the topmost layer of the snowpack in the previous time step, respectively.

Next, the second sub-step - sublimation, denoted by "P2". If the sublimated mass is less than the mass of the topmost layer, then the total number of snow layers will stay the same and the most upper layer mass will be updated as the difference between the mass before sublimation and the sublimated mass. Otherwise, multiple snow layers will be removed from the top of the snowpack such that the total mass of the removed layers is equal to the sublimated mass. The concentration of LAIs in the topmost layer N' after sublimation, $c^{P2}_{LAI,N'}$, is calculated as:

$$c^{P2}_{LAI,N'} = \frac{\sum\limits_{i=N-k_s}^{i=N} c^{P1}_{LAI,i} m^{P1}_i}{\left(\sum\limits_{i=N-k_s}^{i=N} m^{P1}_i\right) - m_{sub}} \tag{2}$$

where m_{sub} is the sublimated mass, k_s is the number of top layers that added up to have a mass equal to/larger to the sublimated mass, $c^{P1}_{LAI,i}$ and m^{P1}_i are the post-snowfall concentration of one of the species and the post-snowfall mass of the i^{th} layer, respectively.

Finally, the last sub-step - melt. Two "melting modes" are implemented to represent two different vertical profiles of snow melt, since the parameterization input is total melt rate of the entire snowpack. The two modes include: "surface melt", which assumes all the meltwater is contributed from the top of the snowpack only, and "uniform melt", in which each snow layer contributes the same fraction of the total melt. The two melting modes provide an uncertainty range for melt: the surface melt mode giving the maximum melt amplification effect while the uniform melt mode giving the minimal effect. For both melting modes, no lateral and vertical water mass transport are assumed and the layers will be merged with the underlying layer if the layer thickness is less than m_{min} after melt. For surface melt mode, the calculation is similar to how sublimation is calculated: a single or multiple snow layers are removed from the top of the snowpack to equal to the total melt thickness. The concentration of LAIs in the post-melt most upper layer N' is dependent on the species-specific meltwater scavenging efficiency, η_{LAI}, which is the fraction of LAI being carried out with the meltwater and related to the size and hydro-properties of the LAI particle. The concentration is calculated as:

$$c_{LAI,N'}(t+1) = \frac{\sum\limits_{i=N-k_m}^{i=N} c^{P2}_{LAI,i} m^{P2}_i}{\sum\limits_{i=N-k_m}^{i=N} m^{P2}_i - m_{melt}} [1 - \eta_{LAI}] \tag{3}$$

m_{melt} is the melted mass, k_m is the number of layers that add up to a mass equal to or larger than the melted mass. $c^{P2}_{LAI,i}$ and m^{P2}_i are the concentration of one of the species and the mass of the i^{th} layer after sublimation, respectively. In the surface melt mode, the layer mass and concentration of LAI of all the underlying layers are assumed to be unchanged after melt.

For uniform melt mode, the post-melt mass of each layer, $m_i(t{+}1)$, is calculated with the post-sublimation mass, m^{P2}_i, and the ratio of the melted height to the total post-sublimation mass as:

$$m_i(t+1) = m^{P2}_i - \Delta m_i = m^{P2}_i - \frac{m^{P2}_i\, m_{melt}}{\sum_{i=1}^{i=N} m^{P2}_i} \tag{4}$$

and the post-melt concentration of the LAIs in each layer is updated based on the post-melt mass of the layer and the scavenging efficiency:

$$c_{LAI,i}(t+1) = \frac{c^{P2}_{LAI,i} m^{P2}_{i} + \eta_{LAI}(c^{P2}_{LAI,i+1}\Delta m_{i+1} - c^{P2}_{LAI,i}\Delta m_i)}{m_i(t+1)} \tag{5}$$

As mentioned earlier, SLAIR estimates the snow surface albedo based on the concentration of LAI in the "near-surface layer", $c_{LAI,ns}$. The concentration of LAIs in the near-surface layer is the same as the concentration of the most upper layer, $c_{LAI,N}$, if its thickness is equal to/larger than the defined near-surface layer thickness, h_{ns} . Otherwise, the concentration of LAIs in the near-surface layer can be calculated by assuming an even distribution of LAI within the near-surface layer:

$$c_{LAI,ns} = \frac{\left(\sum_{i=N-k_{ns}+1}^{i=N} c_{LAI,i}\frac{m_i}{\rho_{s,i}}\right) + c_{LAI,N-k_{ns}}\left(h_{ns} - \sum_{i=N-k_{ns}}^{i=N}\frac{m_i}{\rho_{s,i}}\right)}{h_{ns}} \tag{6}$$

where k_{ns} is the number of snow layers that have a total thickness equal to/larger than h_{ns}, and $\rho_{s,i}$ is the snow density of the i^{th} layer.

2.2 Snow grain size

The evolution of snow effective grain radius - the volume-to-area ratio of snow grain - represents snow aging. The near-surface layer might include snow layers that consist of different snow types: fresh snow, old snow deposited for longer than one day, and refrozen snow which has large ice clumps that have been refrozen from liquid water present within the snowpack. As a result, the overall effective grain radius, r, in the near-surface layer is calculated based on the volume fraction, f, of these three snow types in the near-surface layer at each time step:

$$r(t) = r_f f_f(t) + \left[r_o(t-1) + \frac{dr_o}{dt}\Delta t\right] f_o(t) + r_r f_r(t) \tag{7}$$

where r_f, r_o and r_r is the effective grain radius of fresh, old and refrozen snow, respectively, $\frac{dr_o}{dt}$ is the rate of growth of old snow grain, Δt is the time step, and f_f, f_o and f_r is the fraction of fresh, old and refrozen snow in the near-surface layer.

The effective grain radius of fresh and refrozen snow are fixed while the grain radius of old snow is updated at every time step. The rate of old grain growth is based on the parameterization by Flanner and Zender (2006) for dry grain growth. Liquid water fraction is not included as one of the inputs for simplicity.

The fraction of fresh snow depends on the input value for snowfall while the fraction of old snow depends on the fraction of old plus fresh snow from the previous time step. As mentioned previously, liquid water fraction is not yet accounted for in the current parameterization. The entire near-surface layer, except freshly deposited snow, is defined as refrozen snow whenever the average temperature of the layer is above 0°C.

2.3 Albedo Parameterization

The estimation of snow albedo in the visible band, α_{vis}, is based on works of He, Liou, et al. (2018), Rozenberg (1963), and Malinka et al. (2016) to accommodate various conditions. Details of all three parameterizations can be found in the relevant literature. In brief, the parameterization by He, Liou, et al. (2018) is an empirical formulation for semi-infinite snowpack based on grain size, shape, black carbon equivalent concentration, and LAI-snow mixing scheme. The He, Liou, et al. (2018) parameterization is only applicable for optically thick snowpack. However, parameterizations by Malinka et al. (2016)

and Rozenberg (1963) are both physically based and account for snow optical depth. Malinka et al. (2016) is used for relatively clean but shallow snowpack whereas Rozenberg (1963) is used for heavily contaminated snowpack.

$$\alpha_{vis} = \begin{cases} \text{Malinka et al. (2016)} & \text{if} \quad c_{eqv,ns} < 0.5 \mu\text{g}\,\text{g}^{-1} \;\; \& \;\; \text{snowdepth} \leq 4\text{ cm} \\ \text{Rozenberg (1963)} & \text{if} \quad c_{eqv,ns} \geq 7.5\, \mu\text{g}\,\text{g}^{-1} \;\; \& \;\; \text{r} \geq 900\, \mu\text{m} \\ & \text{or} \quad c_{eqv,ns} \geq 10\, \mu\text{g}\,\text{g}^{-1} \;\; \& \;\; 500 \leq r < 900\, \mu\text{m} \\ \text{He, Liou, et al. (2018)} & \text{otherwise} \end{cases} \tag{8}$$

$c_{eqv,ns}$ is the black carbon equivalent concentration in the near-surface layer, which is calculated:

$$c_{eqv,ns} = c_{BC,ns} + c_{dust,ns} \frac{\sigma_{abs,\text{Dust}}}{\sigma_{abs,\text{BC}}} + c_{OM,ns} \frac{\sigma_{abs,\text{OC}}}{\sigma_{abs,\text{BC}}} \tag{9}$$

The absorption cross-section, σ_{abs}, is as listed in Table. 1. The snow albedo parameterization by He, Liou, et al. (2018) is expressed as:

$$\alpha_{vis}(\theta) = (b_0 + b_1 \log R + b_2 \log R^2) - d_0 (c_{eqv,ns})^{d_1 R^{d2}} \tag{10}$$

where $R = r\,\phi(\theta)/100\mu\text{m}$ is the equivalent radius corrected with solar zenith angle, θ, with $\phi(\theta) = [1 + a\Delta\cos(\theta)]^2$ and $a = 0.781$ for the visible wavelength and $\Delta\cos(\theta) = \cos(\theta) - \cos(49.5°)$. As modeling the evolution of grain shape and LAIs-snow mixing scheme would require detailed internal snow process schemes that are computationally costly, the grain is assumed to be spherical and LAIs are externally mixed such that $b_0 = 9.80508 \times 10^{-1}$, $b_1 = -1.36104 \times 10^{-2}$, $b_2 = -1.95416 \times 10^{-2}$, $d_0 = 3.01470 \times 10^{-3}$, $d_1 = 4.68312 \times 10^{-1}$, and $d_2 = 1.27961 \times 10^{-1}$.

For relatively clean and shallow snow, the albedo parameterization by Malinka et al. (2016) is defined as:

$$\alpha_{vis}(\theta) = (1 - D)\left(1 - \frac{12}{7}\frac{1 + 2\cos(\theta)}{\tau + 4}\right) + D\frac{\tau}{\tau + 4} \tag{11}$$

The parameterization by Rozenberg (1963) for heavily contaminated snow is in a similar form as:

$$\alpha_{vis}(\theta) = (1 - D)\left(\frac{\sinh(\gamma\tau + y[1 - 3/7(1 + 2\cos(\theta))])}{\sinh(\gamma\tau + y)}\right) + D\frac{\sinh(\gamma\tau)}{\sinh(\gamma\tau + y)} \tag{12}$$

where the optical depth, τ, is:

$$\tau = z\,\sigma_{ext,tot}\,\rho_{snow} \tag{13}$$

z is the snow depth, $\sigma_{ext,tot} = \sigma_{ext,ice} + c_{eqv,ns}\sigma_{ext,BC}$ is the total extinction cross-section, D is the fraction of diffuse to the total downward shortwave radiation, γ is the asymptotic attenuation coefficient, and y is defined as:

$$\gamma = \sqrt{3(1 - \omega_0)(1 - \omega_0 g)} \tag{14}$$

$$y = 4\sqrt{\tfrac{1 - \omega_0}{3(1 - \omega_0 g)}} \tag{15}$$

with g = 0.895 as the asymmetric factor, and ω_0 as the single scattering albedo as

$$\omega_0 = \frac{\sigma_{ext,ice}\omega_{ice} + c_{eqv,ns}\sigma_{ext,BC}\omega_{BC}}{\sigma_{ext,tot}} \tag{16}$$

The single scattering albedo of ice, ω_{ice}, and extinction cross-section of ice, $\sigma_{ext,ice}$, is grain size dependent and can be approximated by geometrical optics (Bohren & Huffman, 2007) as:

$$\omega_{ice} = 1 - \tfrac{x T_{\text{diff}}}{x + T_{\text{diff}}} \tag{17}$$

$$\sigma_{ext,ice} = \tfrac{\sigma_{abs}}{1 - \omega_{ice}} \tag{18}$$

where $x = n^2 r\,\sigma_{abs,ice}\rho_{ice}$, with the absorption cross-section of ice, $\sigma_{abs,ice} \sim 5.795 \times 10^{-14}\text{m}^2\,\text{kg}^{-1}$, snow density, $\rho_{ice} = 917\text{kg}\,\text{m}^{-3}$, the real part of the ice refractive index, $n \sim 1.313$, and $T_{\text{diff}} \sim 0.9368$ for the visible wavelength. (Note: Equations used for these approximation are shown in Appendix A).

3 Data and Methods

The new multilayer snow parameterization, SLAIR, is validated by data collected at Col de Porte (45.30°N, 5.77°E; 1325 m a.s.l.), France, by Météo-France during snow-year 2013-2014. This is one of the few publicly available time series of collected in situ measurement of snowfall, runoff, snow albedo, and optical grain size (Morin et al., 2012; Lejeune et al., 2019; Dumont et al., 2017). The validation is separated into two parts: first, evaluating the SLAIR parameterization directly by comparing observed albedo and grain size with results generated by using observed snowfall and runoff as inputs. The second part, we evaluate the overall modeling results by using modeled snowfall and ablation generated by AM4/LM4, a fully-coupled atmospheric-land model, as inputs for SLAIR. Descriptions of the observed and AM4/LM4 modeled data are presented in Sect. 3.1 and 3.2, respectively.

3.1 Observational Data Description

Detailed description of the site and the instrumentation used for all the long-term snow measurements are given in Morin et al. (2012); Lejeune et al. (2019). Spectral measurement details are provided in Dumont et al. (2017). Here, we provide an overview of the parameters that are used for evaluation, including snow physical parameters (e.g. snow depth, snowfall, runoff) and optical parameters (e.g. grain size and spectral albedo).

The snow depth was measured automatically by ultra-sound and laser rangers with a reported accuracy of 1 cm. However, within the experimental site (50×50 m), the spatial variability of measurement bias can be up to ±10 cm. Total daily precipitation was measured by weighing gauges. Snowfall, F_{snowfall}, was partitioned manually with the use of ancillary information and corrected for undercatch depending on the temperature and wind speed. Daily runoff was the average of water mass drained from a 5 m^2 lysimeter. Here, we assumed runoff is equivalent to snowmelt. The uncertainty associated with the runoff data is unclear due to the possible lateral transport in the snowpack and the contribution from rainfall. As sublimation was not measured, therefore, the sublimation flux generated by the AM4/LM4 is used as input.

Spectral albedo was measured with a home-made spectral radiometer at a sub-hourly resolution in the visible and near infrared, which was then converted to flat terrain snow albedo by correcting the slope and aspect of the surface and applying a seasonal scaling factor. The specific surface area (SSA) and impurity content (expressed as black carbon equivalent, BC_{eqv}) of the superficial snow were also retrieved from the spectral measurement for clear-sky days as described in (Dumont et al., 2017). The SSA can be related to the effective grain radius via $r \simeq \frac{3}{\rho_{ice} SSA}$, with ρ_{ice} as the density of ice. For simplicity, here we refer all of the spectral measurements and retrieved parameters as "observed". For the purpose of comparison, all observations are averaged to daily time scale. Besides the spectral measurements, chemical analysis was also carried for the top 27 cm of the snowpack at 3 cm resolution on the 11 February 2014. The concentration of BC and dust were measured with a single particle soot photometer and Coulter counter, respectively.

As the deposition fluxes of aerosol were not measured, the AM4/LM4 modeled aerosol deposition fluxes from the grid point nearest to Col de Porte were used as an input for SLAIR. The dry deposition fluxes were taken directly from the model, while the wet deposition fluxes were scaled to match with the observed snowfall by assuming the atmospheric burden of BC, dust and OM were high enough for this scaling. Description of the modeled aerosols deposition is presented in the next section.

3.2 Modeled Data Description

The fully coupled atmospheric-land global model AM4.0/LM4.0, developed by NOAA's Geophysical Fluid Dynamics Laboratory (GFDL), is used to simulate meteorological parameters, such as surface temperature, flux of solid precipitation, surface sublimation, total snowmelt, and aerosols deposition. Details of the model is presented by Zhao et al. (2018a, 2018b), a brief description is given below focusing on the key model config-urations related to snow and aerosols.

The description of snowpack in the current LM4.0 model is rather simplistic and is the same as LM3 (Milly et al., 2014). The snowpack is represented by five layers, with each layer preassigned a fixed fraction of the total snow depth, which has a minimum depth of 0.01 m w.e.. The rate of sublimation and snowmelt are controlled by the atmosphere-snow-ground heat transport, the net shortwave and longwave radiation at the surface, which are related to the reflectance of the snow surface. The snow albedo parameter-ization used in the current LM4.0 model is a function of surface temperature based on the bidirectional reflectance distribution function (BRDF) albedo model (Schaaf et al., 2002) and does not include radiative feedback of snow darkening by aerosols deposition (Appendix B). Snow compaction is not yet incorporated into the LM4.0 model; a fixed homogeneous snow density is assumed for the entire snowpack. Snow liquid water con-tent is also not yet integrated, i.e. the snowpack does not hold any liquid water and all meltwater is instantly carried through the bottom of the snowpack.

The AM4.0 model simulates the mass distribution of five aerosol types including mineral dust (dust), black carbon (BC), organic carbon (OC), sulfate and sea salt. The aerosol physics in AM4.0 is based on AM3.0, but with a "light" chemistry mechanism designed to simulate sulfate emissions with a prescribed monthly ozone concentrations that calculated from a 20 year climatology (1981-2000) simulated by AM3. The size distribution of dust is represented by five size bins from 0.1 to 10 μm radius while the size dis-tribution of other aerosols is prescribed as lognormal. The atmospheric concentration of aerosols is calculated based on their emission, chemical production for sulfate and secondary organics matters, dry and wet deposition, transport by advection, turbulent diffusion and convection.

Ginoux et al. (2001) parameterization is used to describe lifting of dust particles by wind from dry and barren land. The wind erosion threshold and the global scaling factor were chosen to match the model dust distribution to available observations (Zhao et al., 2018b, and references therein), and is set to be 3.5 ms^{-1} and 0.2 $\mu\mathrm{g\,s}^2\,\mathrm{m}^{-5}$, respectively. The reconstructions of land use/land cover are from CMIP6 forcing. For carbonaceous aerosols (BC and OC) and sulfate precursors, the emission inventories are also obtained from the CMIP6 protocol, which includes emission from natural and anthropogenic combustion of fossil fuel and biofuel. The emitted carbonaceous particles are assumed to be com-posed mostly of hydrophobic (80%) and is converted to hydrophilic by coating with sol-uble materials, e.g. sulfate, as a function of hydroxyl radical concentration, which has an e-folding time ranges from a few hours in heavily polluted urban regions to a few days in clean regions. Aerosols are removed from the atmosphere by dry and wet deposition. Dry deposition includes gravitational settling and impaction at the surface by turbulence. The latter process is treated as deposition velocity, which is parameterized using electric analogy with two resistances in series. Only dust is assumed to be affected by gravitational settling. Aerosols encounter first a wind driven aerodynamic resistance followed by a fixed (100 $\mathrm{s\,m}^{-1}$) viscous surface resistance. Wet deposition includes in-cloud (rain-out) scavenging of hydrophilic particles by incorporating hydrophilic particles into cloud condensate by acting as CNN or IN or by impaction and below-cloud (washout) scav-enging by large-scale precipitation for both hydrophilic and hydrophobic particles. Wet deposition by snowfall is a factor 2 to 4 less than by rainfall, depending on the aerosol type.

For this study, AM4.0/LM4.0 model is run with 33 vertical levels with model stratosphere top at 1 hPa and cubical-sphere topology with 192×192 grid boxes per cube face (approximately 50 km grid size) for the period of 1980-2015 with 1-year simulation as spin-up. To simulate the global distribution of precipitation and reproduce the observed vari-ability of synoptic scale meteorological transport, the simulation is conducted with ob-served sea surface temperature and sea-ice cover taken from the reconstructions of Taylor and Doutriaux (2002) and the wind components are nudged toward NCEP-NCAR re-analysis by Kalnay et al. (1996). Results from the grid point that is nearest to Col de Porte were used for the comparison, which have a modeled elevation of 1224 m a.s.l.

3.3 Simulation setup

For both parts of the SNAIR evaluation, constrained by observed or modeled snowfall and runoff, the same values are used for near-surface layer thickness, snow density, ef-fective grain radius for fresh and refrozen snow, optical and hydro-properties of LAIs.
The near-surface layer, h_{ns}, is defined as the top 3 cm of the snowpack, which is a sufficient thickness for the surface albedo not to be affected significantly by the albedo of the underlying surface/layer in most scenarios. As there is no observed snow density and homogeneous snow density was assumed in the LM4.0 model, to be consistent, snow den-sity of all types of snow, i.e. fresh, old, or refrozen snow, are assumed to be 300 kg m^{-3}. The effective grain radius of fresh and refrozen snow is set to 100 and 1000 μm, respec-tively.

The size distribution and the hydrophilicity of the deposited aerosol particles, which influence the optical properties and scavenging efficiency of the particle, can be provided by the AM4.0 model. However, for simplicity, the optical properties of all three LAIs included in this study were assumed to be homogeneous as listed in Table. 1 (Default).
The scavenging of impurities in snow by meltwater is not yet well quantified. Conway et al. (1996) suggested that particles with size larger than 5 μm are relatively immobile during melt and can be retained at the snow surface even being hydrophilic. However, the relative importance of particle size and hydrophilicity is uncertain. Therefore, the scavenging efficiency of all three LAIs are assumed to be zero to represent the maximum effect of snow darkening. Last but not least, to be comparable with the daily average of observed albedo, the modeled albedo is calculated at insolation-weighted average zenith angle, $\theta = 48.19°$ (Cronin, 2014) and assuming clear-sky condition.

Sensitivity studies on snow density, optical properties of dust, and scavenging efficiency of BC on the calculation of surface BC_{eqv} and snow albedo by SLAIR in surface melt mode using observed precipitation and runoff as inputs, all the values used for the sen-sitivity test is listed in Table. 1. Snow density of 200, 400, and 500 kgm^{-3} are selected to represent fresher, windpacked, and melting snow. The optical properties of dust has the most variability and uncertainty due to its large range of particle size that can vary from tenths of nanometers to hundreds of microns., and chemical composition, such as Hematite (Fe_2O_3) content. Therefore, optical properties of four other types of dust par-ticle that corresponding to 0.9% and 2.7% Fe_2O_3 and in the size range of $0.1 - 1$ and $6 - 10$ μm are chosen for the sensitivity study.

The scavenging efficiency depends on the size and hydrophobicity of the particle, for ex-ample a small hydrophilic particle has a higher scavenging efficiency than a large hydropho-bic particle (Conway et al., 1996). In general, BC particles are much smaller in size com-pared to dust particles and the majority of emitted BC particles are hydrophobic. Note: BC particles can convert to hydrophilic by acquiring hygroscopic materials with an e-folding time of tens of hours. Thus, scavenging efficiency of 20% is set for all BC par-ticles in the sensitivity test. Last but not least, the observed grain size and BC_{eqv} have been interpolated linearly to daily resolution and fed directly into the albedo parameterization (as shown in Sect. 2.3) to assess its sensitivity to grain size and BC_{eqv} concentration.

4 Results and Discussion

4.1 Snowfall & snow depth

The AM4/LM4 model captured most of the snowfall events throughout the entire snow season (Fig. 2a, with modeled in red and observed in grey), however, the magnitude of the solid precipitation flux is much lower in the model compared with observations. The low bias in modeled snowfall is the most likely linked to the spatial resolution of the model (50 km), leading to elevation errors which resulted in a low orographic snowfall bias due to lower total precipitation and a larger percentage of precipitation falling as rain in the model (Kapnick & Delworth, 2013a; Kapnick et al., 2014, 2018). Furthermore, the low elevation bias in the model grid cell (1224 ma.s.l) compared to the measurement site (1325 ma.s.l) can also prompt slightly higher elevation-related temperature within in the model. For runoff (Fig. 2b), no similarity can be found in the temporal variation or the magnitude between the modeled (in red) and observed (in grey). Generally, the simulated runoff has a smaller magnitude than the observed, except from mid-January to mid-March when the melt rates are comparable between the two. The automatic snow depth measurements (Fig. 2c in grey × on the left axis), the estimated snow depth from observed precipitation and runoff (Fig. 2c in dark grey line on the left axis), and modeled snow depth by AM4/LM4 (Fig. 2c in red line on the right axis) all show a similar temporal trend. Snowpack starts to build up slowly from mid November, reaches maximum snow depth in early March, and then has a second peak in late March. However, the melt-out date of the modeled snowpack is 5 days earlier than the automatic measurements and 15 days earlier the estimation using the observed precipitation and runoff. The modeled snow depth is roughly 5 times lower than the observed at its peak. The mismatch in the melt-out date between the automatic measurement and estimation using observed precipitation and runoff is due to the spatial variability of the measurement field (Lejeune et al., 2019) and the uncertainty in runoff, especially towards to end of the season of which rainfall might have contributed to the runoff. Whereas for the model, the shorter snow season and underestimation of snow depth can be explained by the combination of the low snow precipitation, the relatively high runoff with respective the snowfall, and the assumption of a constant (time-independent and vertically homogeneous) snow density.

4.2 Aerosol deposition flux

The total deposition flux of aerosols as BC_{eqv} is shown in Fig. 2d, with red as the outputs from the AM4/LM4 model and grey as the “estimated deposition flux” used for the run with observed snowfall and runoff. The total “estimated deposition flux” is higher than the flux from AM4/LM4 since the wet deposition has been scaled to the observed snowfall, which is higher than the modeled snowfall (Fig. 2a). As the dry deposition was assumed to be the same in the “estimated deposition flux”, the total deposition flux between the two are similar at the beginning and toward the end of the snow season when the deposition is governed by dry deposition. The estimated wet and dry deposition flux of BC and dust used for the run with observed snowfall and runoff are shown in Fig. 3a and 3b, respectively. At Col de Porte, the deposition of BC is continuous and governed by wet deposition (shaded black) while the deposition of dust is intermittent and a mix of wet (shaded orange) and dry deposition (shaded yellow). Two major wet deposition events of dust ($\sim$24-46 $\mathrm{mg\,m^{-2}}$) occurred on 2 February and 23 March and minor events ($\sim$0.8-4 $\mathrm{mg\,m^{-2}}$) happened between 16-19 January and on 7, 10, 12 and 15 February. For dry deposition of dust, two significant events outbreaks ($\sim$12-76 $\mathrm{mg\,m^{-2}}$) occurred on 17 February and from 28 March to 4 April. The timing of these major dust deposition events is consistent with the deposition flux simulated from the regional atmospheric model ALADIN-Climate but with a one or two day shift (Tuzet et al., 2017). The Dust REgional Atmospheric model (BSC-DREAM8b) also predicted a significant amount of dust deposition (~50-100 mg m^{-2}) around 18 February at Lecco, Italy, a site located approximately 200 km East of Col de Porte at a similar elevation of 1650 m (Di Mauro et al., 2015).

4.3 Surface concentration of BC_{eqv}

Fig. 4a shows the near-surface BC_{eqv} concentration simulated using observed precipi-tation and runoff, and scaled modeled aerosol deposition flux as inputs. The concentra-tion simulated by surface melt mode (red solid-line) has a better fit with observations (grey × with error bar indicating the standard deviation) throughout the entire snow season than the uniform melt mode (red dashed-line) as indicated by the NRMSE (root-mean-square errors normalized by the standard deviations of the observations) listed in Table 2. During the accumulation phase, the surface BC_{eqv} concentrations simulated by the two melting modes are not too dissimilar to each other: they exibit a similar tem-poral trend as observations despite an underestimation in mid-January and overestima-tion in both mid-February and early March. The chemical analysis of snow samples on the 11 February shows the concentration of dust and BC in the top 3 cm of the snow-pack are 149 and 16 ng g^{-1}, respectively (Tuzet et al., 2017). The simulated concentra-tion of dust on the 11 February underestimated by ~5 times with surface melt mode and ~6 times with uniform melt mode while the simulated concentration of BC is overesti-mated by ~1.5 times with uniform melt mode and ~1.7 times with surface melt mode. However, on the 12 February, the simulated concentration of dust is only ~2 times lower than the measurement on the 11 February. This behavior could be due to the slight time shift of the modeled dust deposition event.

The difference between the two melting modes become significant when substantial melt-ing started to occur from April onward (Fig. 2c). During the final ablation phase, the BC_{eqv} concentration estimated by the surface melt mode agreed well with the observa-tions while the uniform melt mode underestimated the surface concentration by up to an order of magnitude and does not reproduce the observed temporal pattern. Thus, the NRMSE during the ablation period is significantly lower for the surface melt mode com-pared to the uniform melt mode (Table 2). The spectral measurements ended 11 days before the melt-off day of the snowpack estimated from the observed precipitation and runoff. However, the final simulated surface concentration is comparable (~15 % higher) with the observation. Overall, as a result of continuous deposition of BC and its high absorptivity, BC is the dominant LAI in the near-surface layer in both surface and uni-form melt mode (Fig. 3c & 3d). The contribution of dust to the total BC_{eqv} concentra-tion increased at the final ablation period due to the significant dry deposition of dust in late March through early April.

During the accumulation phase, the surface melt (red solid-line) and uniform melt (red dashed-line) mode using modeled precipitaiton and runoff as boundary conditions resulted in a similar concentration in BC_{eqv} in the near-surface layer (Fig. 5a). Both underes-timated the surface concentration in mid-January while overestimated in mid-February. The results from the two melting modes start to deviate significantly from mid-March onward, a month earlier compared with the run with observed precipitation and runoff, when the majority of the precipitation comes to a halt. During the ablation phase, in contrast to the simulation using observed snowfall and runoff, the BC_{eqv} concentration simulated by the uniform melt mode has a better agreement with observations than sur-face melt mode, with the simulated concentration up to an order of magnitude higher.

The concentration of BC_{eqv} at the near-surface layer is governed by the aerosol depo-sition flux during the accumulation phase. The close match between the simulated BC_{eqv} concentration using observed (Fig. 4a) and modeled (Fig. 5a) inputs, despite the low bias in snowfall in the model (Fig. 2b), suggested that the wet deposition flux is the controlling factor for the near-surface LAI concentration during the accumulation phase. Though, in early to mid-January, there is a week-long substantial melting (Fig. 2c) conjoined with a week-long absence of snowfall (Fig. 2b) which lead to significant surface LAI enhancement and resulted in a high surface concentration. Therefore, the underestimation of surface concentration in mid-January is likely to be the combined effect of underestimation in runoff and dry deposition flux. For the run with observed inputs, the uncertainty in runoff can be arise from the spatial variation in runoff at the measurement site, i.e. difference in the quantity of melt at where runoff were measured and where the spectral measurements were made. Meanwhile, the overestimation in $\mathrm{BC}_{\mathrm{eqv}}$ concentration in mid-February using either observed or modeled snowfall and runoff as inputs is probably due to the overestimation in the LAI deposition flux.

During the ablation period, the surface concentration of $\mathrm{BC}_{\mathrm{eqv}}$ is governed by runoff and the surface concentration enhancement induced by melt. The difference between the two melting modes indicates that the surface concentration does not only depend on the amount of melt but also where it happens within the snowpack. This is especially evident in thicker snowpack, shown by the differences between the runs with observed and modeled precipitation and runoff as inputs. Principally, snowmelt is controlled by several processes: 1) net incoming solar radiation, which depends on the incoming radiation and surface albedo; 2) transfer of sensible heat from overlying atmosphere and the ground below, which depends on air and ground temperature, wind speed, snow density, and the liquid water content within the snowpack; 3) transfer of latent heat through sublimation and condensation; and 4) heat transfer by rain. For thick snowpack, melt is predominately controlled by net solar radiation as snow is a relatively nonconductive medium (i.e. heat transfer within the snowpack can be slow) particularly in low temperatures or low wind conditions. Therefore, for the run with the observed precipitation and runoff as inputs, which have a maximum snow depth over 1.5 m (Fig. 2c), the majority of melt is likely to happen at the surface due to absorption of solar radiation. In contrast, modeled snow depth is only ∼20% of observed snow depth. The vertical distribution of melt is likely to be more even across the snowpack as relatively less time is required to transport available heat through the entire snowpack.

4.4 Effective grain size

The grain size simulated with observed inputs (Fig. 4b as red ∘) and modeled inputs (Fig. 5b as red ∘), both follow the general temporal pattern of observed grain size (grey × with an error bar indicating the standard deviation). Both of the simulated grain sizes mainly remain within the uncertainties of observed values during the accumulation phase. The one exception is the overestimation in mid-January when surface temperature went above 0°C (in turquoise dash-line on right axis). In early to mid-March and from April onward, the observed grain size increases gradually and follows a similar trend to the surface temperature. However, in contrast the simulated grain size was set to the maximum grain size for most of this time as the temperature stayed above 0°C. In late March when the surface temperature went below zero and snow fell for a couple of days in observations and the model (Fig. 2), the simulated grain size is comparable with the observed but with a slightly slower rate of growth.

In the real world, grain metamorphism can be categorized into three mechanisms: equitemperature growth, kinetic growth and wet metamorphism (Lehning et al., 2002). Equitemperature growth metamorphism is governed by the water vapor gradient between surfaces due to different radii of curvature at the ice interface under a small temperature gradient. Kinetic growth metamorphism is driven by the water vapor gradient between the ice matrix and pore space under a large temperature gradient. Wet metamorphism is determined by the liquid water content of the snowpack when the temperature is just below or at its melting point and liquid water is redistributed among the grains.

The growth rate by wet metamorphism is positively correlated with the liquid water content and is much more rapid compared to equitemperature growth due to the fast diffusion rate of liquid water compared to water vapor (Brun, 1989). In SLAIR, there is no tracking of liquid water or wet grain growth. The entire near-surface layer is assumed to be refrozen and set to the maximum grain size whenever the average temperature of the layer is 0°C or above. Therefore, the current effective grain size parameterization included in SLAIR can only provide a reasonable snow grain evolution for regions that have a surface temperature below freezing for the entire snow season and contains only dry snow. For areas that have an average surface temperature above freezing, the parameterization is likely to overestimate the grain size at the beginning of the ablation period and underestimate towards the end of the season. In our model results, this leads to an overestimation in mid-January and absence of detailed variations in grain size during the ablation period.

4.5 Snow albedo

Fig. 4c shows the observed (grey × with error bar representing the standard deviation) and simulated snow albedo in the visible using observed precipitation and runoff in surface melt mode (red solid-line) and uniform melt mode (red dashed-line). Overall, the simulated albedo by surface melt mode is more comparable to observations for the entire snow season as suggested by the NRSME listed in Table 3. During the accumulation phase, the simulated albedo by the two melting modes is very similar. They both have a temporal pattern closely matching observations. The two exceptions of overestimation occur in: (a) early January due to the combination of an underestimation in BC_{eqv} (Fig 4a) and overestimation in snow grain size (Fig 4b), and (b) a few days in February when low albedo with relatively large uncertainties were recorded. During the ablation phase, the magnitude of simulated albedo by the surface melt mode is very close to that observed. In contrast, the albedos simulated in the uniform melt mode only have good agreement in the early part of the ablation phase but are significantly overestimated in the final phase of ablation as a result of the underestimation in BC_{eqv} concentration.

Fig. 5c shows that the temporal variation of simulated albedo generally agrees with observations during the accumulation phase and early ablation phase for both the surface and uniform melt mode, except for the underestimation in late February due to the overestimation in BC_{eqv} concentration (Fig. 5a). From mid-March onwards the albedo estimated by the surface melt mode generally agrees with the temporal pattern but with smaller magnitude, especially during the final ablation phase. The uniform melt mode however captured both the pattern and magnitude of observed albedo.

The albedo estimated by BRDF, the parameterization that is currently adopted in the AM4/LM4 model, is also shown in Fig. 5c in turquoise. The albedo is underestimated by BRDF parameterization throughout the snow season until the final ablation period when it is overestimated. The BRDF parameterization estimates the albedo by linearly interpolating a cold (< -10°C) and warm (> 0°C) snow albedo and does not take any snow darkening feedback into account (See Appendix B for more details). Therefore, the albedo underestimation during the majority of the snow season is due to the relatively warm temperature at Col de Porte (Fig. 5b in turquoise on right axis). The overestimation at the final ablation period is due to the lack of LAI-induced albedo reduction. The underestimation of surface albedo by BRDF increases the surface absorbed solar radiation and increases air temperature, leading to a high rate of melt. This might explain the relatively high melt rate with respect to snowfall in the model.

As mentioned previously, the surface snow albedo is governed by the size of the snow grain when the concentration of LAIs is low, therefore, the albedo simulated by either melting modes or with observed or modeled precipitation and runoff as inputs, are very similar during accumulation phase when the LAIs concentration is low. However, during the ablation phase, when the concentration of LAIs increases due to the melt-induced sur-face concentration enhancement, the concentration of LAIs becomes the predominant factor that determines the snow albedo. Hence, the differences in albedo estimated by the two melting modes or with observed or modeled inputs can be significant, particu-larly during the final ablation period.

4.6 Sensitivity Analysis

All of the sensitivity runs were performed with observed precipitation and runoff in sur-face melt mode, with different sets of parameters such as snow density, optical properties of dust, and scavenging efficiency. Table 2 compares the BC$_{\mathrm{eqv}}$ concentration responses to the parameters listed above. The concentration of BC$_{\mathrm{eqv}}$ is not sensitive to snow den-sity during the accumulation phase. The average precipitation flux (excluding zero val-ues) during the accumulation phase is $\sim$9.60 kg m^{-2} day^{-1}, which is equivalent to a fresh snow depth of $\sim$1.9-4.8 cm for snow density ranged between 200-500 kgm^{-3}. Therefore for the majority of the accumulation phase, the near-surface layer–set to 3 cm–mainly consisted of freshly fallen snow regardless of the snow density. Hence the near-surface concentration is predominantly determined by the concentration of BC$_{\mathrm{eqv}}$ in the fresh snow. The agreement between observations and simulated BC$_{\mathrm{eqv}}$ concentration improved significantly during the ablation phase when the snow density increased from 300 to 500 kg m $^{-3}$. Generally, snow becomes denser as it ages or with depth or when melting; there-fore, having a higher snow density might be closer to reality. The assumption of homo-geneous density throughout the entire snow season might lead to large uncertainties in the concentration of BC$_{\mathrm{eqv}}$, especially during ablation.

Changing the optical properties of dust does not have a substantial impact on the over-all concentration of BC$_{\mathrm{eqv}}$ during both the accumulation and ablation phases. This is likely linked to the relatively small contribution of dust to the total absorption at the surface at Col de Porte. BC is the dominant LAIs throughout the snow season even though the contribution of dust to the total LAIs at the near-surface increased at the final ab-lation period (Fig. 3). From Eq. 2.3, the BC$_{\mathrm{eqv}}$ concentration would be more sensitive to the optical properties of dust if it had a higher concentration relative to BC. In the future, with the combination of declining BC emission due to mitigation protocols and increasing dust emission due to the increase of climate change-induced drought and continuous change of land use, the role of dust in snow darkening might become more prominent so that the variations in dust optical properties should be taken into consideration.

As expected, the BC$_{\mathrm{eqv}}$ concentration does not respond to the change of scavenging efficiency of BC during accumulation phase as the amplification by melt is limited and the near-surface concentration is governed by the flux of precipitation and aerosols deposi-tion. During ablation, melt amplification plays an important role in near-surface con-centration, increasing the scavenging efficiency of BC from 0% to 20% improved the fit to the observed BC$_{\mathrm{eqv}}$ concentration slightly. In reality, it is likely that a portion of the BC particles are hydrophilic so that they can be washed away with meltwater. However, to estimate that accurately, first, we would have to treat the deposition of hydrophilic and hydrophobic LAI particles separately in the parameterization; this would require us to have information about the types of LAI particles instead of bulk values currently mod-eled in our GCM. Secondly, we would have to constrain the value of scavenging efficiency of different particles through controlled experiments. This detailed work is outside the scope of this study.

The albedo of snow in the visible band is not sensitive to any of the tested parameters (Table 3). Even though the improvement in the estimation of BC$_{\mathrm{eqv}}$ concentration is significant during ablation by assuming a larger snow density, the improvement in the estimation of snow albedo is minor. In order to directly assess the sensitivity of the snow albedo parameterization to grain size and concentration of BC$_{\mathrm{eqv}}$, a simulation was run using the linearly interpolated observed grain size and BC_{eqv} concentration. The simulated albedo (Fig. 4b, pink line) improved slightly during the accumulation phase by reproducing the dip in mid-January. The results are similar to the default run during ablation. As mentioned in the Introduction, besides grain size and LAI concentration, the snow albedo is also dependent on the grain shape and the mixing scheme between the LAI and ice crystal. These parameters are not yet taken into account when estimating the snow albedo, which can induce uncertainty (He, Flanner, et al., 2018). Furthermore, there are uncertainties associated with the observed surface albedo due to factors such as: surface slope, aspect, clouds cover and presence of liquid water. Given our ability to roughly reproduce albedo with the given parameterization, these uncertainties are a smaller order than snow age at the surface and LAI concentration.

4.7 Summary

In this study, we have developed a simple snow parameterization - SLAIR to simulate surface albedo based on the evolution of grain size and light-absorbing impurities in snow. The parameterization was evaluated against a set of publicly available field data in the French Alps during the snow year 2013-2014. The simulated snow visible albedo is in good agreement with observations when the parameterization is driven by observed snow-fall and runoff and with surface melt mode, which assumed all the melting happens at the surface of the snowpack. This initial evaluation shows the SLAIR parameterization provided a significant improvement in the estimation of snow surface albedo in compar-ison to the BRDF model, a parameterization currently adopted by the GFDL AM4/LM4 climate model, by improving the description of snow aging and incorporating the radia-tive feedback of snow darkening by the deposition of LAIs.

The parameterization as it stands can provide a reasonable estimation in near-surface BC_{eqv} concentration, snow grain size, and snow visible albedo for an area with a mean surface temperature below refreezing for the entire snow season and have reasonable estimation in the snow precipitation. However, the SLAIR parameterization still has its limitations, especially during the melt season. Further developments are required to minimize uncertainties.

5 Future work and development

The lack of liquid water content description in the snow parameterization has compro-mised the detailed variation in snow grain size. Including liquid water content as one of the input parameters is expected to improve the modeling of grain size and fraction of refrozen snow. This would allow wet grain growth to be incorporated into the param-eterization. This additional input parameter is most beneficial when estimating snow dark-ening in relatively warm regions with a surface temperature above freezing and infrared snow albedo, which is more sensitive to the snow grain size.

The two melting modes presented here–surface melt and uniform melt–provide a range of uncertainties that related to where melt occurs within the snowpack as the parameterization is constrained by the total runoff to minimize computational cost. However, this uncertainty can be rather large, especially for relatively thick snowpack. To strike a balance between the computational efficiency and accuracy, the snow parameterization should take into account additional parameters such as the percentage runoff from each layer within the coarse vertical resolution large scale model to get a better percep-tion on which part of snowpack contributes the most to runoff.

The sensitivity test suggested it is insufficient to assume a homogeneous snow density for the entire snow season. A paramterization of snow density that correlates with compression, temperature, and liquid water content should be implemented, i.e. Anderson (1976); Boone and Etchevers (2001); Lynch-Stieglitz (1994). However, the snow density parameterization in SLAIR should be made consistent with the one being used within the large scale model. Furthermore, particles with different hydro-properties and opti-cal properties should be treated separately in the parameterization to further reduce uncertainty relating to their washing out with meltwater runoff.

The differences in BC_{eqv} concentration and visible albedo when using observed and modeled snowfall and runoff as inputs indicated that cumulative snowfall is a crucial param-eter for generating a good estimation, especially towards the end of the snow season. It is critical to validate the parameterization with other local-scaled observations of LAIs as well as remote sensing data to further understand the limitation of the parameter-ization.

Table 1: The optical properties of BC, dust and organic matter in the visible wavelength (300-700 nm)

Properties	BC	Dust (Default)	OC	Dust (0.9% Fe_2O_3)		Dust (2.7% Fe_2O_3)		Units
				0.1-1 μm	6-10 μm	0.1-1 μm	6-10 μm	
Single scatter albedo, ω	0.209	0.857	0.963	0.984	0.773	0.969	0.611	dimensionless
Extinction cross-section, σ_{ext}	9267	474	3289	2091	78.2	2182	78.2	m^2kg^{-1}
Scattering cross-section, σ_{sct}	1937	406	3167	2056	60.4	2115	47.9	m^2kg^{-1}
Absorption cross-section, σ_{abs}	7330	67.8	122	33.4	17.8	67.3	30.5	m^2kg^{-1}

Table 2: NRMSE between the observed surface concentration of black carbon equivalent, BC_{eqv}, and SLAIR estimation using observed precipitation and runoff (using modeled precipitation and runoff) in both the surface and uniform melt mode under "Default". For the result of the sensitivity tests, NRMSE is between observed BC_{eqv} concentration and SLAIR estimation using observed precipitation and runoff as inputs with different values for density, optical properties of dust, and scavenging efficient of BC.

Period	Default[a]		ρ_{snow}, kg m^{-3}			Dust (0.9% Fe_2O_3)		Dust (2.7% Fe_2O_3)		η_{BC}
	Surf	Uni	200	400	500	0.1-1 μm	6-10 μm	0.1-1 μm	6-10 μm	20 %
Entire (6/Jan-13/Apr)	0.69 (3.04)	1.09 (2.43)	1.11	0.53	0.48	0.68	0.67	0.71	0.68	0.65
Accumulation (6/Jan-5/Mar)	1.11 (1.19)	1.06 (0.90)	1.07	1.08	1.04	1.10	1.10	1.11	1.10	1.10
Ablation (6/Mar-13/Apr)	0.64 (3.40)	1.15 (2.72)	1.17	0.41	0.33	0.62	0.61	0.66	0.62	0.56

[a] Default have a snow density of 300 kg m^{-3} and the optical properties as listed in the first 3 column of Table 1.

Table 3: NRMSE between the observed snow visible albedo and SLAIR estimation using observed precipitation and runoff (using modeled precipitation and runoff) in both the surface and uniform melt mode under "Default". For the result of the sensitivity tests, NRMSE is between observed albedo and SLAIR estimation using observed precipitation and runoff as inputs with different values for density, optical properties of dust, scavenging efficient of BC, and with observed grain size and BC_{eqv} concentration.

Period	Default[a]		ρ_{snow}, kg m^{-3}			Dust (0.9% Fe_2O_3)		Dust (2.7% Fe_2O_3)		η_{BC}	Obs r
	Surf	Uni	200	400	500	0.1-1 μm	6-10 μm	0.1-1 μm	6-10 μm	20 %	Obs BC_{eqv}
Entire (6/Jan-13/Apr)	0.85(1.32)	1.19(1.01)	0.93	0.83	0.83	0.85	0.85	0.85	0.85	0.85	0.82
Accumulation (6/Jan-5/Mar)	1.20(1.18)	1.21(1.10)	1.21	1.19	1.19	1.20	1.20	1.20	1.20	1.21	1.14
Ablation (6/Mar-13/Apr)	0.63(1.64)	1.34(1.00)	0.83	0.59	0.61	0.62	0.62	0.63	0.62	0.63	0.63

[a] Default have a snow density of 300 kg m^{-3} and the optical properties as listed in Table 1.

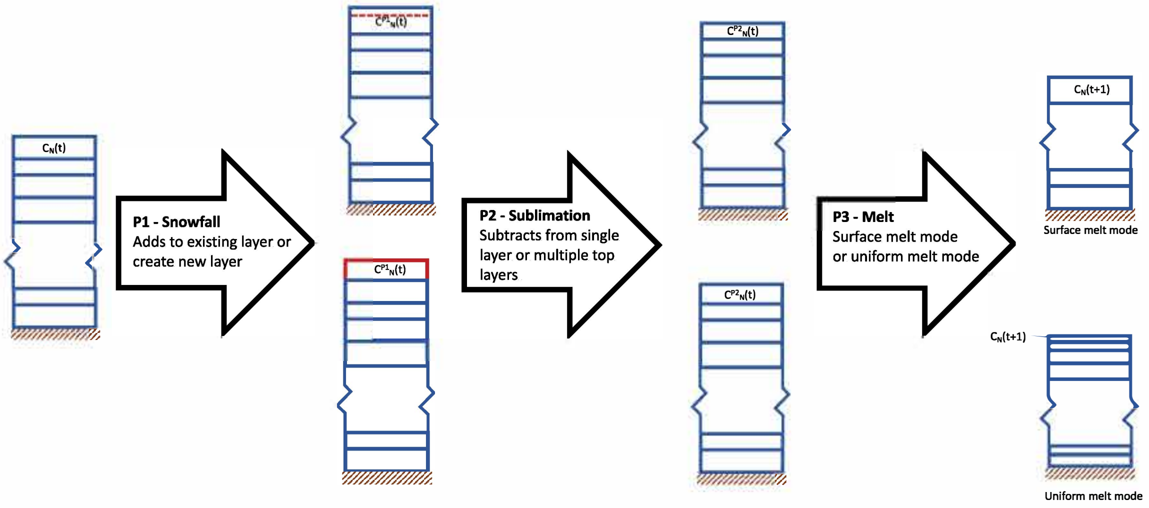

Figure 1: Schematic diagram of numerical scheme for calculating the concentration of LAIs in each layer. The calculation is separated into three sub-processes, Process 1 (P1)-snowfall, Process 2 (P2) - sublimation, and Process 3 (P3) - melt.

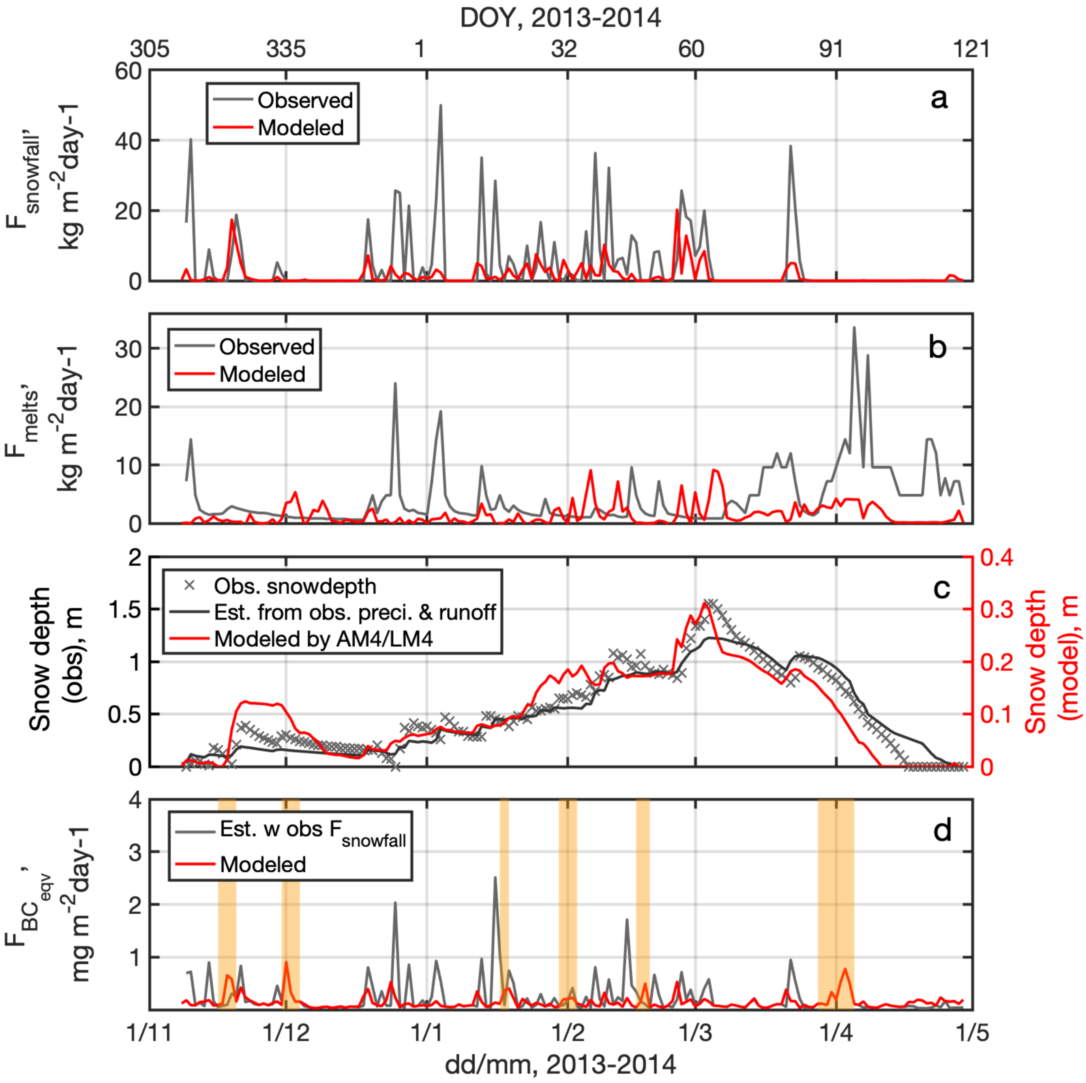

Figure 2: (**a**) Flux of solid precipitation (snowfall) at Col de Porte, France for the 2013-2014 snow year, with grey line as the observed flux and red line as the modeled flux. (**b**) Flux of snow melt (runoff), with grey line as the observed flux and red line as the modeled flux. (**c**) Snow depth, with grey × (left axis) as the observed auto-measured snow depth (Lejeune et al., 2019), dark grey line (left axis) as the snow depth estimated from the observed snowfall and runoff (Lejeune et al., 2019) by assuming a constant snow density of 300 kg m^{-3}, and red line (right axis) as the snow depth calculated from modeled snowfall and ablation from AM4.0/LM4.0 by assuming a constant snow density of 300 kg m^{-3}; (**d**) Total deposition flux of BC equivalent (BC + dust + OM), with grey line as modeled deposition flux that been scaled to observed precipitation and red line as the model flux. Major dust events are represented by the orange shading.

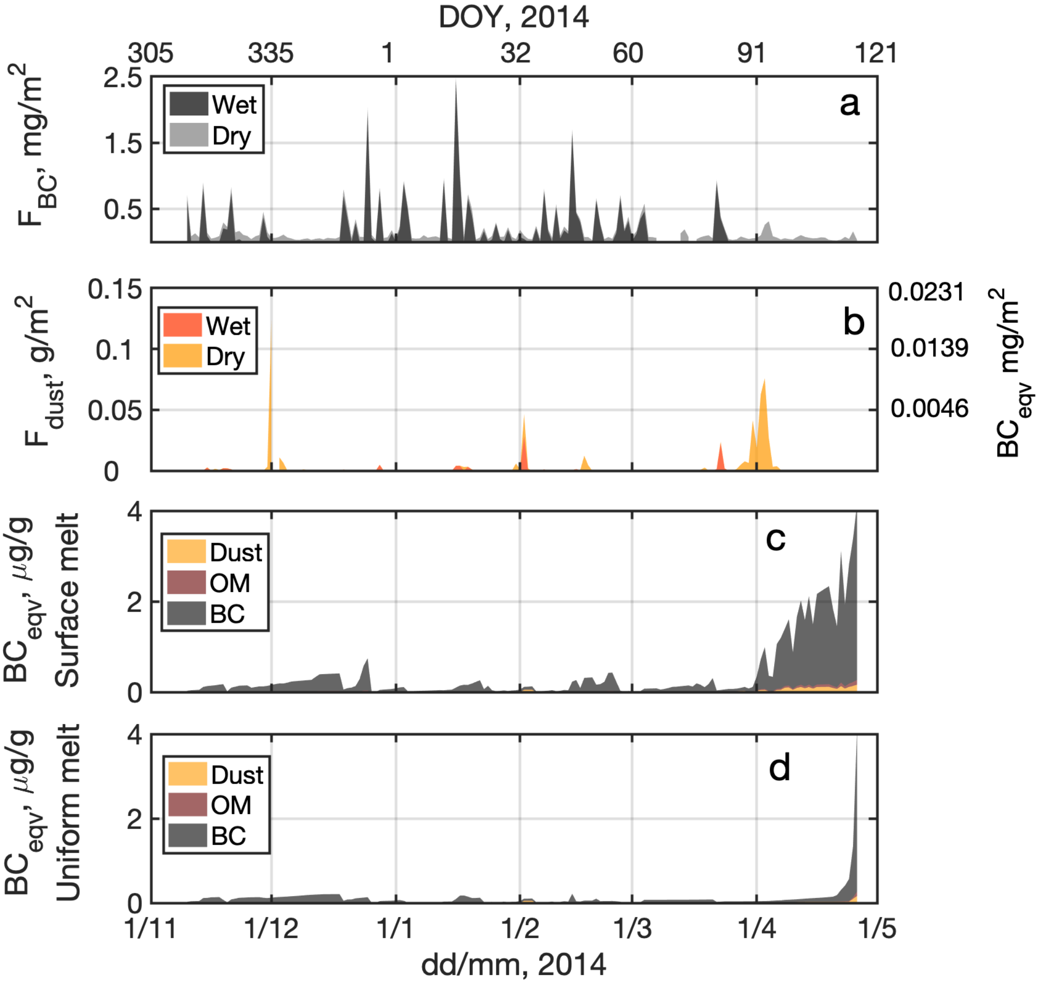

Figure 3: Aerosol deposition flux used for the simulation with observed precipitation and runoff; (**a**) deposition flux of BC with black as modeled wet deposition flux that scaled to the observed solid precipitation and grey as modeled dry deposition flux; (**b**) deposition flux of dust with orange as modeled wet deposition flux that scaled to the observed solid precipitation and yellow as modeled dry deposition flux. The deposition flux as BC_{eqv} is plotted on the right axis; And the concentration of BC_{eqv} at the near-surface layer simulated (**c**) in surface melt mode; (**d**) in uniform melt mode with orange, brown and black as the concentration of dust, OM, and BC, respectively.

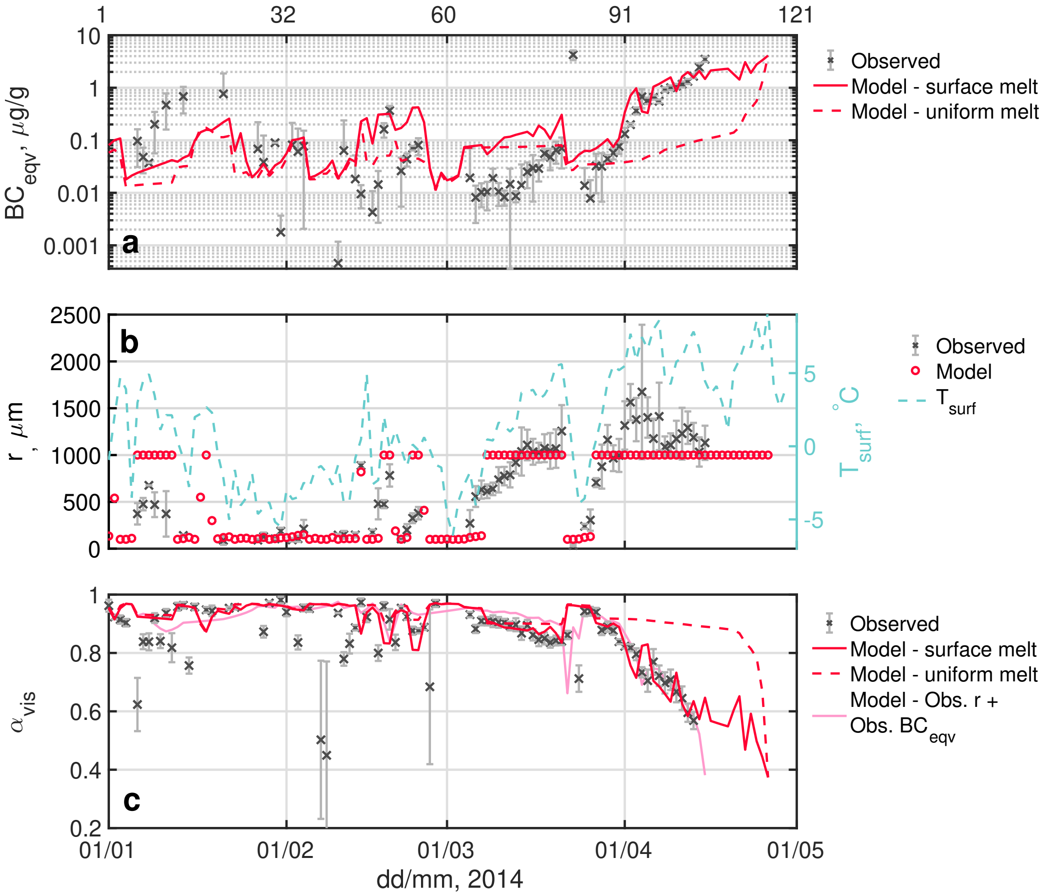

Figure 4: Results by SLAIR using observed snow precipitation and runoff with (**a**) surface concentration of BC equivalent, BC$_{\text{eqv}}$, with grey × as daily mean (± standard deviation), red dash-line and solid-line as modeled in uniform melt mode and surface melt mode, respectively; (**b**, left axis) the effective grain size, r, with grey × as the observed daily mean (± standard deviation), and red ∘ as the modeled; (**b**, right axis) surface temperature modeled by AM4/LM4, in turquoise; (**c**) snow surface visible albedo, α_{vis}, with grey × as the observed daily mean albedo at 550 nm (± standard deviation), red dash-line and solid-line as modeled in uniform melt mode and surface melt mode, respectively; pink ∘ as albedo estimated with the SLAIR albedo parameterization (Sect. 2.3) using observed grain size and BC$_{\text{eqv}}$.

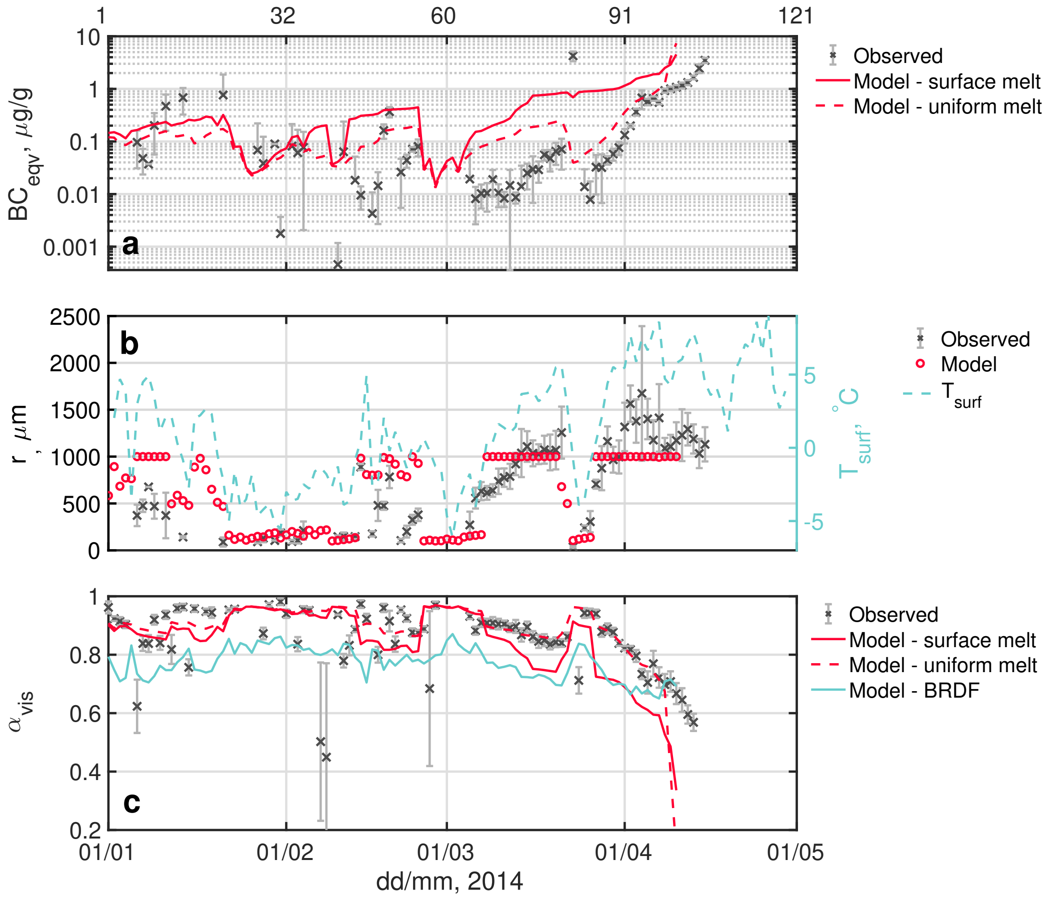

Figure 5: Results by SLAIR using AM4/LM4 precipitation and ablation with (**a**) surface concentration of BC equivalent, BC$_{\text{eqv}}$, with grey × as daily mean (± standard deviation), red dash-line and solid-line as modeled in uniform melt mode and surface melt mode, respectively; (**b**, left axis) the effective grain size, r, with grey × as the observed daily mean (± standard deviation), and red ∘ as the modeled; (**b**, right axis) surface temperature modeled by AM4/LM4, in turquoise; (**c**) snow surface visible albedo, α_{vis}, with grey × as the observed daily mean albedo at 550 nm (± standard deviation), red dash-line and solid-line as modeled in uniform melt mode and surface melt mode, respectively; turquoise line as albedo calculated by BRDF parameterization embedded in the current LM4.0 model.

Appendix A Optical Properties of ice

The optical properties of ice can be approximated by geometrical optics (Bohren & Huffman, 2007) using the ice refractive index, $m = n + i\kappa$, with n and κ being the real and imaginary part, respectively, i.e. (Warren & Brandt, 2008). The absorption cross-section, $\sigma_{abs,ice}$, can be approximated as

$$\sigma_{abs,ice} = \frac{4\pi\kappa}{\lambda}\frac{1}{\rho_{ice}} \tag{A1}$$

where λ is the wavelength and ρ_{ice} as density of ice. The single-scattering albedo of ice, ω_{ice}, as

$$\omega_{ice} = 1 - \frac{xT_{\mathrm{diff}}}{x + T_{\mathrm{diff}}} \tag{A2}$$

with

$$x = n^2 r\, \sigma_{abs}\rho_{ice} \tag{A3}$$

$$\begin{aligned} T_{\mathrm{diff}} = \quad & \tfrac{2(5n^6+8n^5+6n^4-5n^3-n-1)}{3(n^3+n^2+n+1)(n^4-1)} + \\ & \tfrac{n^2(n^2-1)^2}{(n^2+1)^3} \ln \tfrac{n+1}{n-1} - \tfrac{8n^4(n^4+1)}{(n^4-1)^2(n^2+1)} \ln n \end{aligned} \tag{A4}$$

Appendix B AM4.0/LM4.0 snow albedo parameterization

The snow albedo parameterization that currently adopted by the GFDL LM4.0 is based on the bidirectional reflectance distribution function (BRDF) albedo model (Schaaf et al., 2002). The black-sky (direct-light, α_{bs}) and white-sky (diffuse light, α_{ws}) albedo are defined as:

$$\begin{aligned} \alpha_{bs}(\theta) =& f_{iso}(g_{0,iso} + g_{1,iso}\theta^2 + g_{2,iso}\theta^3) \qquad \text{(B1)} \\ &+ f_{vol}(g_{0,vol} + g_{1,vol}\theta^2 + g_{2,vol}\theta^3) \\ &+ f_{geo}(g_{0,geo} + g_{1,geo}\theta^2 + g_{2,geo}\theta^3) \\ \alpha_{ws} =& f_{iso}g_{iso} + f_{vol}g_{vol} + f_{geo}g_{geo} \qquad \text{(B2)} \end{aligned}$$

where the f values are the wavelength dependent "snow type" constants, g values are the universal parameters of BRDF model, and θ is the solar zenith angle in radian. Two different f values are used within LM4 to represent snow type in "cold" (below -10°C) and "warm" (above 0°C) conditions (Table. Appendix B). Within this 0- -10°C range the snow reflectances are linear interpolated with temperature. The overall albedo can then be calculated from the black and white sky albedo with the ratio between diffuse-to-total downward shortwave radiation, D, as

$$\alpha(\theta) = (1 - D)\alpha_{bs}(\theta) + D\alpha_{ws} \tag{B3}$$

Acknowledgments:
The research was supported by the NASA HiMAT project, NASA grant 15-HMA15-0016. Data and code used in this paper will be made available at ftp://data1.gfdl.noaa.gov/users/Sarah.Kapnick/HiMAT/and https://nsidc.org/data/highmountainasia/.
Hoi Ga Chan is currently affiliated with the Port of London Authority, London, United Kingdom.
Sarah Kapnick is currently affiliated with NOAA HQ, Washington DC 20230, USA.

Table B1: Snow type constant in the visible wavelength and universal parameters of BRDF reflectance parameterization

	iso	vol	geo
g_0	1.0	-0.007574	-1.284909
g_1	0.0	-0.070987	-0.166314
g_2	0.0	0.307588	0.041840
g	1.0	0.189184	-1.377622
f (cold)	0.92	0.06	0.0
f (warm)	0.77	0.06	0.0

References

Anderson, E. A. (1976). Noaa technical report nws ; 19. Retrieved from `https://repository.library.noaa.gov/view/noaa/6392`

Bohren, C. F., & Huffman, D. R. (2007). Geometrical optics. In *Absorption and scattering of light by small particles* (pp. 166–180). Wiley-VCH Verlag GmbH. Retrieved from `http://dx.doi.org/10.1002/9783527618156.ch7` doi: 10.1002/9783527618156.ch7

Boone, A., & Etchevers, P. (2001). An intercomparison of three snow schemes of varying complexity coupled to the same land surface model: Local-scale evaluation at an alpine site. *Journal of Hydrometeorology*, *2*(4), 374-394.

Brown, M., Racoviteanu, A., Tarboton, D., Gupta, A. S., Nigro, J., Policelli, F., … Tokar, S. (2014). An integrated modeling system for estimating glacier and snow melt driven streamflow from remote sensing and earth system data products in the himalayas. *Journal of Hydrology*, *519*, 1859 - 1869. Retrieved from `http://www.sciencedirect.com/science/article/pii/S002216941400732X` doi: https://doi.org/10.1016/j.jhydrol.2014.09.050

Brun, E. (1989). Investigation on wet-snow metamorphism in respect of liquid-water content. *Annals of Glaciology*, *13*, 22–26. doi: 10.3189/S0260305500007576

Conway, H., Gades, A., & Raymond, C. F. (1996). Albedo of dirty snow during conditions of melt. *Water Resources Research*, *32*(6), 1713-1718. Retrieved from `https://agupubs.onlinelibrary.wiley.com/doi/abs/10.1029/96WR00712` doi: 10.1029/96WR00712

Cronin, T. W. (2014). On the choice of average solar zenith angle. *Journal of the Atmospheric Sciences*, *71*(8), 2994-3003. Retrieved from `https://doi.org/10.1175/JAS-D-13-0392.1` doi: 10.1175/JAS-D-13-0392.1

Di Mauro, B., Fava, F., Ferrero, L., Garzonio, R., Baccolo, G., Delmonte, B., & Colombo, R. (2015). Mineral dust impact on snow radiative properties in the european alps combining ground, uav, and satellite observations. *Journal of Geophysical Research: Atmospheres*, *120*(12), 6080-6097. Retrieved from `https://agupubs.onlinelibrary.wiley.com/doi/abs/10.1002/2015JD023287` doi: 10.1002/2015JD023287

Doherty, S. J., Grenfell, T. C., Forsström, S., Hegg, D. L., Brandt, R. E., & Warren, S. G. (2013). Observed vertical redistribution of black carbon and other insoluble light-absorbing particles in melting snow. *Journal of Geophysical Research: Atmospheres*, *118*(11), 5553-5569. Retrieved from `https://agupubs.onlinelibrary.wiley.com/doi/abs/10.1002/jgrd.50235` doi: 10.1002/jgrd.50235

Dumont, M., Arnaud, L., Picard, G., Libois, Q., Lejeune, Y., Nabat, P., … Morin, S. (2017). In situ continuous visible and near-infrared spectroscopy of an alpine snowpack. *The Cryosphere*, *11*(3), 1091–1110. Retrieved from `https://www.the-cryosphere.net/11/1091/2017/` doi: 10.5194/tc-11-1091-2017

Dutra, E., Balsamo, G., Viterbo, P., Miranda, P. M. A., Beljaars, A., Schär, C., & Elder, K. (2010). An improved snow scheme for the ecmwf land surface model: Description and offline validation. *Journal of Hydrometeorology*, *11*(4), 899-916. Retrieved from `https://doi.org/10.1175/2010JHM1249.1` doi: 10.1175/2010JHM1249.1

Estilow, T. W., Young, A. H., & Robinson, D. A. (2015). A long-term northern hemisphere snow cover extent data record for climate studies and monitoring. *Earth System Science Data*, *7*(1), 137–142. Retrieved from `https://www.earth-syst-sci-data.net/7/137/2015/` doi: 10.5194/essd-7-137-2015

Flanner, M. G., & Zender, C. S. (2006). Linking snowpack microphysics and albedo evolution. *Journal of Geophysical Research: Atmospheres*, *111*(D12), n/a–n/a. Retrieved from `http://dx.doi.org/10.1029/2005JD006834` (D12208) doi: 10.1029/2005JD006834

Flanner, M. G., Zender, C. S., Hess, P. G., Mahowald, N. M., Painter, T. H., Ramanathan, V., & Rasch, P. J. (2009). Springtime warming and reduced snow cover from carbonaceous particles. *Atmospheric Chemistry and Physics*, *9*(7), 2481–2497. Retrieved from `https://www.atmos-chem-phys.net/9/2481/2009/` doi: 10.5194/acp-9-2481-2009

Ginoux, P., Chin, M., Tegen, I., Prospero, J. M., Holben, B., Dubovik, O., & Lin, S.-J. (2001). Sources and distributions of dust aerosols simulated with the gocart model. *Journal of Geophysical Research: Atmospheres*, *106*(D17), 20255-20273. Retrieved from `https://agupubs.onlinelibrary.wiley.com/doi/abs/10.1029/2000JD000053` doi: 10.1029/2000JD000053

Hadley, O. L., & Kirchstetter, T. W. (2012). Black-carbon reduction of snow albedo. *Nature Climate Change*, *2*(6), 437–440. Retrieved from `https://doi.org/10.1038/nclimate1433` doi: 10.1038/nclimate1433

He, C., Flanner, M. G., Chen, F., Barlage, M., Liou, K.-N., Kang, S., ... Qian, Y. (2018). Black carbon-induced snow albedo reduction over the tibetan plateau: uncertainties from snow grain shape and aerosol–snow mixing state based on an updated snicar model. *Atmospheric Chemistry and Physics*, *18*(15), 11507–11527. Retrieved from `https://www.atmos-chem-phys.net/18/11507/2018/` doi: 10.5194/acp-18-11507-2018

He, C., Liou, K., Takano, Y., Yang, P., Qi, L., & Chen, F. (2018). Impact of grain shape and multiple black carbon internal mixing on snow albedo: Parameterization and radiative effect analysis. *Journal of Geophysical Research: Atmospheres*, *123*(2), 1253–1268. Retrieved from `http://dx.doi.org/10.1002/2017JD027752` (2017JD027752) doi: 10.1002/2017JD027752

Kalnay, E., Kanamitsu, M., Kistler, R., Collins, W., Deaven, D., Gandin, L., ... Joseph, D. (1996). The ncep/ncar 40-year reanalysis project. *Bulletin of the American Meteorological Society*, *77*(3), 4370472.

Kapnick, S. B., & Delworth, T. L. (2013a). Controls of global snow under a changed climate. *Journal of Climate*, *26*(15), 5537–5562.

Kapnick, S. B., & Delworth, T. L. (2013b, 2019/10/30). Controls of global snow under a changed climate. *Journal of Climate*, *26*(15), 5537–5562. Retrieved from `https://doi.org/10.1175/JCLI-D-12-00528.1` doi: 10.1175/JCLI-D-12-00528.1

Kapnick, S. B., Delworth, T. L., Ashfaq, M., Malyshev, S., & Milly, P. C. (2014). Snowfall less sensitive to warming in karakoram than in himalayas due to a unique seasonal cycle. *Nature Geoscience*, *7*(11), 834.

Kapnick, S. B., Yang, X., Vecchi, G., Delworth, T. L., Gudgel, R., Malyshev, S., ... Margulis, S. (2018). Potential for western us seasonal snowpack prediction. *Proceedings of the National Academy of Sciences*, *115*(6), 1180–1185.

Lawrence, D. M., Fisher, R. A., Koven, C. D., Oleson, K. W., Swenson, S. C., Bonan, G., ... Zeng, X. (2019). The community land model version 5: Description of new features, benchmarking, and impact of forcing uncertainty. *Journal of Advances in Modeling Earth Systems*, *0*(ja). Retrieved from `https://agupubs.onlinelibrary.wiley.com/doi/abs/10.1029/2018MS001583` doi: 10.1029/2018MS001583

Lehning, M., Bartelt, P., Brown, B., Fierz, C., & Satyawali, P. (2002). A physical snowpack model for the swiss avalanche warning: Part ii. snow microstructure. *Cold Regions Science and Technology*, *35*(3), 147 - 167. Retrieved from `http://www.sciencedirect.com/science/article/pii/S0165232X02000733` doi: https://doi.org/10.1016/S0165-232X(02)00073-3

Lejeune, Y., Dumont, M., Panel, J.-M., Lafaysse, M., Lapalus, P., Le Gac, E., ... Morin, S. (2019). 57 years (1960–2017) of snow and meteorological observations from a mid-altitude mountain site (col de porte, france, 1325 m of altitude). *Earth System Science Data*, *11*(1), 71–88. Retrieved from `https://www.earth-syst-sci-data.net/11/71/2019/` doi: 10.5194/essd-11-71-2019

Lynch-Stieglitz, M. (1994, 2019/09/26). The development and validation of a simple snow model for the giss gcm. *Journal of Climate*, *7*(12), 1842–1855. Retrieved from `https://doi.org/10.1175/1520-0442(1994)007<1842:TDAVOA>2.0.CO;2` doi: 10.1175/1520-0442(1994)007⟨1842:TDAVOA⟩2.0.CO;2

Malinka, A., Zege, E., Heygster, G., & Istomina, L. (2016). Reflective properties of white sea ice and snow. *The Cryosphere*, *10*(6), 2541–2557. Retrieved from `https://www.the-cryosphere.net/10/2541/2016/` doi: 10.5194/tc-10-2541-2016

Milly, P. C. D., Malyshev, S. L., Shevliakova, E., Dunne, K. A., Findell, K. L., Gleeson, T., … Swenson, S. (2014, 2019/11/12). An enhanced model of land water and energy for global hydrologic and earth-system studies. *Journal of Hydrometeorology*, *15*(5), 1739–1761. Retrieved from `https://doi.org/10.1175/JHM-D-13-0162.1` doi: 10.1175/JHM-D-13-0162.1

Morin, S., Lejeune, Y., Lesaffre, B., Panel, J.-M., Poncet, D., David, P., & Sudul, M. (2012). An 18-yr long (1993,§?2011) snow and meteorological dataset from a mid-altitude mountain site (col de porte, france, 1325 m alt.) for driving and evaluating snowpack models. *Earth System Science Data*, *4*(1), 13–21. Retrieved from `https://www.earth-syst-sci-data.net/4/13/2012/` doi: 10.5194/essd-4-13-2012

Rozenberg, G. V. (1963). Optical properties of thick layers of a homogeneous scattering medium. *Spectroscopy of light scattering media, Academy of Sciences of the BSSR, Minsk*, 5-35.

Schaaf, C. B., Gao, F., Strahler, A. H., Lucht, W., Li, X., Tsang, T., … Roy, D. (2002). First operational brdf, albedo nadir reflectance products from modis. *Remote Sensing of Environment*, *83*(1), 135 - 148. Retrieved from `http://www.sciencedirect.com/science/article/pii/S0034425702000913` (The Moderate Resolution Imaging Spectroradiometer (MODIS): a new generation of Land Surface Monitoring) doi: https://doi.org/10.1016/S0034-4257(02)00091-3

Skiles, S. M., Flanner, M., Cook, J. M., Dumont, M., & Painter, T. H. (2018). Radiative forcing by light-absorbing particles in snow. *Nature Climate Change*, *8*(11), 964–971. Retrieved from `https://doi.org/10.1038/s41558-018-0296-5` doi: 10.1038/s41558-018-0296-5

Taylor, K. E., & Doutriaux, C. (2002). *An objective method for generating land/sea masks for use in gcm simulations* (PCMDI Report No. 58). UNIVERSITY OF CALIFORNIA.

Tuzet, F., Dumont, M., Lafaysse, M., Picard, G., Arnaud, L., Voisin, D., … Morin, S. (2017). A multilayer physically based snowpack model simulating direct and indirect radiative impacts of light-absorbing impurities in snow. *The Cryosphere*, *11*(6), 2633–2653. Retrieved from `https://www.the-cryosphere.net/11/2633/2017/` doi: 10.5194/tc-11-2633-2017

Vionnet, V., Brun, E., Morin, S., Boone, A., Faroux, S., Le Moigne, P., … Willemet, J.-M. (2012). The detailed snowpack scheme crocus and its implementation in surfex v7.2. *Geoscientific Model Development*, *5*(3), 773–791. Retrieved from `https://www.geosci-model-dev.net/5/773/2012/` doi: 10.5194/gmd-5-773-2012

Warren, S. G. (1982). Optical properties of snow. *Reviews of Geophysics*, *20*(1), 67-89. Retrieved from `https://agupubs.onlinelibrary.wiley.com/doi/abs/10.1029/RG020i001p00067` doi: 10.1029/RG020i001p00067

Warren, S. G., & Brandt, R. E. (2008). Optical constants of ice from the ultraviolet to the microwave: A revised compilation. *Journal of Geophysical Research: Atmospheres*, *113*(D14). Retrieved from `https://agupubs.onlinelibrary.wiley.com/doi/abs/10.1029/2007JD009744` doi: 10.1029/2007JD009744

Zhao, M., Golaz, J., Held, I. M., Guo, B. V., H., Benson, R., & et al. (2018a). The gfdl global atmosphere and land model am4.0/lm4.0: 1. simulation characteristics with prescribed ssts. *Journal of Advances in Modeling Earth Systems*, *10*, 691-734. Retrieved from `https://doi.org/10.1002/2017MS001208` doi: 10.1002/2017MS001208

Zhao, M., Golaz, J., Held, I. M., Guo, B. V., H., Benson, R., & et al. (2018b). The gfdl global atmosphere and land model am4.0/lm4.0: 2. model description, sensitivity studies, and tuning strategies. *Journal of Advances in Modeling Earth Systems*, *10*, 735-769. Retrieved from `https://doi.org/10.1002/2017MS001209` doi: 10.1002/2017MS001209